Intrinsic anisotropy versus effective pinning anisotropy in YBa_{2}Cu_{3}O_{7} thin films and nanocomposites

E. Bartolomé, F. Vallés, A. Palau, V. Rouco, N. Pompeo, F. F. Balakirev, B. Maiorov, L. Civale, T. Puig, X. Obradors, and E. Silva

Phys. Rev. B **100**, 054502 — Published 2 August 2019

DOI: 10.1103/PhysRevB.100.054502

Intrinsic anisotropy *versus* effective pinning anisotropy in $YBa_2Cu_3O_7$ thin-films and nanocomposites

E. Bartolomé[1*], F. Vallés[2], A. Palau[2], V. Rouco[2], N. Pompeo[3], F.F. Balakirev[4], B. Maiorov[4], L. Civale[4], T. Puig[2], X. Obradors[2], E. Silva[3]

[1] *Escola Universitaria Salesiana de Sarrià (EUSS), Passeig Sant Joan Bosco 74, 08017-Barcelona, Spain*
[2] *Institut de Ciència de Materials de Barcelona-CSIC, Campus UAB, 08193-Bellaterra, Spain*
[3] *Dipartimento di Ingegneria, Università Roma Tre, Via Vito Volterra 62, 00146, Roma, Italy*
[4] *Material Physics and Application Division, Los Alamos National Laboratory, 87545, Los Alamos, USA*

(Received xxxxxx, Accepted for publication xxxxxx, Published xxxxxx)

The intrinsic and effective anisotropies, both in the liquid and solid vortex regimes, of $YBa_2Cu_3O_7$ pristine and nanocomposite thin-films have been investigated. Angular resistivity measurements under varying fields and temperatures were performed to characterize the intrinsic *vs.* effective anisotropy of samples in the regime of long-range vortex displacements. The effective anisotropy γ_{eff} was determined from the scaling of the irreversibility line, applying Blatter approach developed for uniaxial anisotropic superconductors. Resistive measurements in flux-flow were utilized, in addition to H_{c2} measurements in ultra-high-fields, to determine the intrinsic anisotropy mass γ, enabling the study of a large number of samples with varied nanoparticle compositions. In order to access the intrinsic anisotropy in the vortex solid phase, complex impedance measurements at high microwave frequencies were performed, allowing us to access the flux-flow intrinsic anisotropy in the regime of very-short vortex oscillations within the pinning potential wells. Results show that while the effective anisotropy γ_{eff} decays as the nanoparticles-induced nanostrain in the YBCO films increases, the intrinsic anisotropy γ(determined both in dc and at microwave frequency) remains unaltered.

DOI:

I. INTRODUCTION

At present, different strategies for inducing effective vortex pinning centers in $YBa_2Cu_3O_{7-x}$ (YBCO) thin-films have been demonstrated. Attending to the structural dimensionality of the pinning centers, they are usually classified as 0D (vacancies, substitutional atoms), 1D (dislocations, irradiation tracks), 2D (stacking faults, antiphase boundaries, twin boundaries, grain boundaries) and 3D (voids and secondary phases)[1]. One of the most successful approaches for improving the performance of YBCO has been the addition of non-superconducting secondary phases. An important issue under discussion is the effect of the added nanocenters on the angular anisotropy of the superconducting properties in nanocomposites grown by different methods.

The electronic mass anisotropy is an *intrinsic* property of YBCO that depends on the crystalline structure and electronic properties of the material, and is given by the ratio $\gamma=(m_c/m_{ab})^{1/2}$, where m_{ab} and m_c are the effective masses along the *ab* and *c* directions. In a single band superconductor, γ is temperature independent and the angular dependence of the superconductor coherence length is given by $\xi(\theta)=\varepsilon(\theta)\xi_{ab}$, with $\varepsilon(\theta)=[\cos^2\theta+\gamma^2\sin^2\theta]^{1/2}$, thus $\xi_c=\xi_{ab}/\gamma$. This anisotropy can be determined from the angular dependence of different physical magnitudes such as the upper critical field H_{c2}, and the flux-flow resistivity ρ_{ff} in the vortex-liquid state, provided it is far from the solid-liquid transition[2]. It has been shown that in the presence of point-like disorder, the solid liquid transition can be also scaled using $\varepsilon(\theta)$[2,3].

On the other hand, the angular dependence of properties determined by the vortex pinning landscape (such as critical current densities, irreversibility fields and flux creep rates) is more complex. Clearly, pinning by 1D and 2D centres is strongly directional, introducing additional angular dependences. Blatter [4] proposed a general scaling approach for vortex matter in uniaxial anisotropic superconductors. In particular, it predicts that the irreversibility line should scale as $H_{irr}(\theta,T)=\varepsilon(\theta)\ H_{irr}(0,T)$ and the critical current density as $J_c(T,\theta,H)=J_c(T,0,\varepsilon(\theta)H)$. These behaviours have been confirmed experimentally in YBCO[5–9], but the obtained anisotropy does not always coincide with the intrinsic anisotropy γ. This motivated the definition of an empirical *effective* anisotropy, γ_{eff}, and a generalized angular factor $\varepsilon_{eff}(\theta)=[\cos^2\theta+\gamma_{eff}^{-2}\sin^2\theta]^{1/2}$. There is clear evidence that γ_{eff} in YBCO is influenced by the presence of 3D disorder such as nanoparticles. It is thus an *extrinsic* parameter, which depends not only on the crystalline properties of the clean material, but also on the disorder in each sample.

In the last years, the ICMAB group reported on solution-derived YBCO nanocomposites (NCs) including different types of nanoparticles, exhibiting very strong, isotropic pinning [6]. These nanocomposites follow the anisotropic

*ebartolome@euss.es

scaling approach over broad angular regions, with a significantly smaller effective anisotropy (e.g. γ_{eff} =1.4 for a 13% $BaZrO_3$ (BZO) NC) than that of pristine samples, deploying γ_{eff} =5-7[6]. The decreased value of γ_{eff} correlates with the increase in the isotropic nanostrain in the material, associated with the large number of intergrowths emerging from incoherent interfaces between the random NPs and the YBCO matrix [10]. It has been suggested that the effective pinning defects may consist of non-superconducting nanoregions created by Cooper pair suppression under tensile stress, according to the bond contraction pairing (BCP) model[6].

To clarify whether the decreased anisotropy was truly related to the strained lattice and not to a modification of the intrinsic electronic properties of the NC, the intrinsic anisotropy γ of a 13%BZO NC was determined through the determination of H_{c2} at **H**//*c* and **H**//*ab* under very high pulsed magnetic fields. The intrinsic anisotropy of the NC, γ~5.9-6.0, was similar to that of the pristine sample, thus a modification of the electronic properties was excluded[6].

In recent years, the influence of nanodefects on the effective anisotropy, as well as on the $H_{c2}(T)$ dependence and the intrinsic γ has been a matter of discussion, as apparently different phenomenology exists:

The reduction of the effective anisotropy γ_{eff} has been further observed in different types of nanostructured superconducting thin-films: trifluoracertate (TFA) metal-organic (MOD) derived $GdBa_2Cu_3O_y$+$BaHfO_3$ (GdBCO-BHO)[11], Chemical Solution Deposition (CSD) grown Gd_2O_3+$GdBa_2Cu_3O_y$[12], and Metalorganic Chemical Vapor Deposition (MOCVD) grown YBCO with BZO nanorods[13]. In these works, the intrinsic anisotropy was not reported.

The group of Labalestier investigated the anisotropy properties of pulsed laser deposition (PLD) grown YBCO films containing either Y_2O_3 NPs or stacking faults (SFs)[14]. A larger reduction of the effective anisotropy was observed for the Y_2O_3 films (γ_{eff}=3) than for the SF-containing samples (γ_{eff}≈5), as a consequence of the enhanced isotropic pinning in the former, while the intrinsic anisotropy was similar for both types of samples (γ=5-7), thus confirming that disorder does not affect the electronic properties of the material.

Recently, the anisotropy of MOD-prepared YGdBaCuO films with BZO has been discussed [15]: here again, the addition of NPs did not affect the intrinsic anisotropy (γ=5.0). However, different from other reported MOD-grown YBCO with BZO NPs[6,16], a reduction of the effective anisotropy was not observed, a result explained by the presence of a higher density of twin boundaries.

Besides, it has been shown that the addition of nanodefects affects $H_{c2}(T)$ in a varied manner: while no changes in H_{c2} are produced in some cases [17], an increase in H_{c2} with the concentration of defects has been reported in others (e.g. our YBCO+NP[6], YGdBCO+BHO and BZO-doped coated conductors[18]). We note here that such an increase does not necessarily imply a change in the intrinsic anisotropy (i.e. the *ratio* γ=ξ_{ab}/ξ_c). However, the group of Paturi has reported raised values of $H_{c2}(T)$ and a decrease of the intrinsic angular anisotropy to γ≈3 for PLD-grown YBCO thin-films including a small 4-8%wt. of $BaCeO_3$ (BCO)[19] or BZO[20,21] nanoparticles. In these works the effects of the NPs on γ_{eff} were not discussed. In recent years, the effects of strong-pinning produced e.g. by spherical inclusions[22,23] on the anisotropy of uniaxial anisotropic superconductors[24] has been theoretically investigated.

In the present work we have further investigated the intrinsic and effective anisotropy of CSD-grown YBCO nanocomposites, both in the regime of long-range vortex displacements (in dc) and the range of fast, short-range oscillations at microwave frequencies. The investigations of different regimes is important: in dc one can access the onset of the dissipation with J_c and H_{irr}, that are nonlinear dynamic phenomena and are necessarily affected by all details of pinning and vortex phases, and the flux-flow regime. The latter, in dc, is accessible only at high fields and/or high temperatures and/or high transport currents. A clean dc flux-flow regime is usually confined to a very narrow region of the (*H,T,J*) space. All of the dc measurements are based on the vortex drag over significant distances. To have access to complementary information, vortex "shaking" at very high (microwave) frequency, producing very small oscillations, can be used by detecting the complex response and extracting the flux-flow resistivity in the vortex solid state, that is at lower fields and very small currents (details in Sec. IV).

Resistive measurements in the flux-flow regime were utilized, in addition to H_{c2} measurements in ultra-high-fields, as an alternative, faster method to determine the intrinsic anisotropy γ, allowing us to expand our study to a large number of samples with varied nanoparticle compositions. In addition, complex impedance measurements under microwave frequencies were used to obtain the flux-flow resistivity in the vortex solid phase at different field orientations, hence the anisotropy. The angular dependence and the anisotropy of the different superconducting observables, determined by the different methods, as a function of the increased sample nanostrain induced by the nanoparticles is discussed.

II. EXPERIMENTAL METHODS

Epitaxial *c*-axis-oriented YBCO thin-films and nanocomposites (thickness 180-200 nm) were grown on single-crystalline 5×5 mm^2 $LaAlO_3$ (LAO) substrates by using a metal–organic decomposition method based on the TFA route [14]. For this study we considered NCs including different types of secondary phases: $BaZrO_3$ (BZO), Y_2O_3 (YO), Ba_2YTaO_6 (BYTO) and BYTO+Cu. Details on the

sample preparation can be found in previous works [10]. We showed that for all these NCs, the increase in the incoherent specific interface introduced by the nanoparticles correlates with the sample nanostrain (%). The YBCO thin-films and NCs were chosen so as to span a broad nanostrain range between 0.08-0.28 %. Nanostrain was determined by exploiting XRD integral-breadth measurements through semiquantitative Williamson-Hall method [10].

For resistive measurements narrow bridges in the range of 10-30 μm were patterned by standard optical lithography. Silver metal contacts were evaporated and post-annealed, to assure a good contact resistance. Electric transport measurements were performed in a 4-point bridge configuration, in a PPMS Quantum Design system provided with a 9 T magnet, variable temperature from 5-300 K and a rotator with 0.1° resolution. Angular measurements were carried out by rotating the sample around a horizontal axis with an angle θ varying from 0° (**H**//c) to 90° (**H**//ab). Resistance measurements were performed using an AC-current of 10 μA and 33 Hz. The normal state resistivity, $\rho_N(T)$, was determined from the linear fit of the $\rho(T)$ curve measured at H=0 in the ohmic regime (T>150 K). The transition of the resistivity to zero in the absence of applied field (H=0), and at different fields served to determine, respectively, the critical temperature T_c and the irreversible temperature $T_{irr}(H)$ curve.

The criterium used to determine T_c and T_{irr} was $\rho_{crit}=10^{-3}\rho(100\ K)$. The effective anisotropy of samples (γ_{eff}) was determined using Blatter scaling from the analysis of the irreversibility line $H_{irr}(T, \theta)$ obtained from angular resistive data, $\rho(H,T,\theta)$. In addition, from the analysis of resistive measurements in the flux-flow regime, $\rho_{ff}(H,T,\theta)$, the intrinsic anisotropy, $\gamma_{Hc2,res}$ could be obtained.

Angular-dependent resistivity measurements in pulsed magnetic fields up to 65 T, with pulse duration of 50 ms, were carried out at the National High Magnetic Field Laboratory at Los Alamos National Laboratory, following the same protocols described in refs.[3,25]. The sample was mounted in the maximum Lorentz force configuration on a rotation sample holder, and measured at different angles from 0° (**H**//c) to 90° (**H**//ab). The experimental data were recorded on a digitizer using a high-resolution low-noise synchronous lock-in technique with an applied ac electric current of 10 μA and 110 kHz along the bridge. The value of H_{c2} at a given T was determined from the intersection field between the linear fit of $R(H)$ in the normal state and the linear (flux-flow) region of $R(H)$ during the transition. These measurements allowed us obtaining the angular anisotropy of the upper critical field, denoted, $\gamma_{Hc2,HF}$. We note here that the obtained value is independent of the particular criterium used to determine H_{c2}.

High-frequency measurements were performed by means of the dielectric resonator technique on unpatterned samples. We measured the transmission scattering coefficient of a sapphire-loaded dielectric resonator[26] operating at f=47.3 GHz, as a function of the applied magnetic field $\mu_0 H \leq 0.8$ T and the field orientation. The resulting resonance curve was fitted to a Lorentzian curve with the appropriate corrections[27] to obtain the unloaded quality factor Q and the resonant frequency f_0 as a function of H and θ, at different T. The field variation of Q and f_0 are directly related to the field or angle variation of the surface impedance $Z=R+iX$ according to[28]:

$$\Delta Z_S(H) = Z_S(H) - Z_S(0) = G\left[\frac{1}{Q(H)} - \frac{1}{Q(0)} + 2i\frac{f_0(H) - f_0(0)}{f_0(0)}\right], \quad (1)$$

where G is a calculated geometrical factor. Considering the problem of the high frequency response in the mixed state in tilted fields for isotropic[29,30] and anisotropic superconductors[31,32], an expression for the high frequency complex resistivity γ_{MW} is available[32,33]. In addition, since the films are thinner than a few London penetration depth, the effective surface impedance is, to a very good approximation[34], given by:

$$Z_S = \frac{\rho_{MW}}{t_s} = \frac{\rho_1(H,\theta,T) + i\rho_2(H,\theta,T)}{t_s}, \quad (2)$$

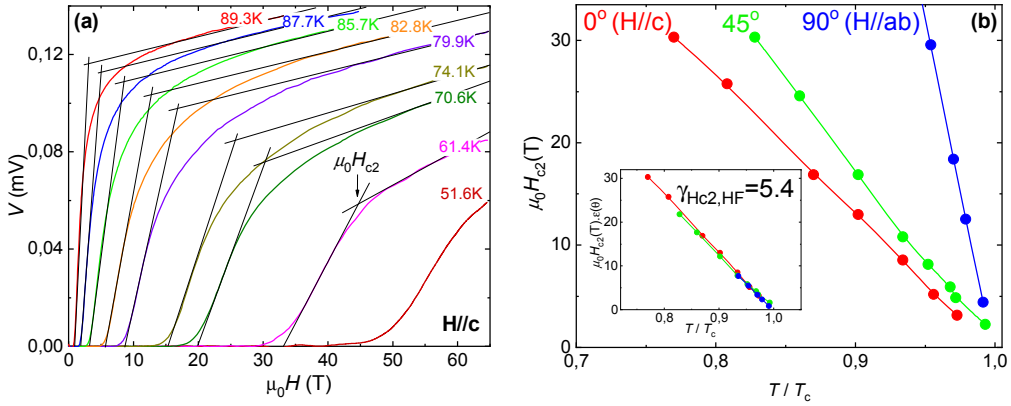

FIG. 1. (a) Isothermal $R(H)=V(H)/I$ measurements made in pulsed magnetic fields up to 65 T. The determination procedure of $\mu_0 H_{c2}$ is indicated; (b) $\mu_0 H_{c2}$ as a function of the reduced temperature for different magnetic field orientations. Inset: collapse of the three curves using an intrinsic $\gamma_{Hc2,res}$=5.4±0.3. (Sample: 15%BYTO nanocomposite).

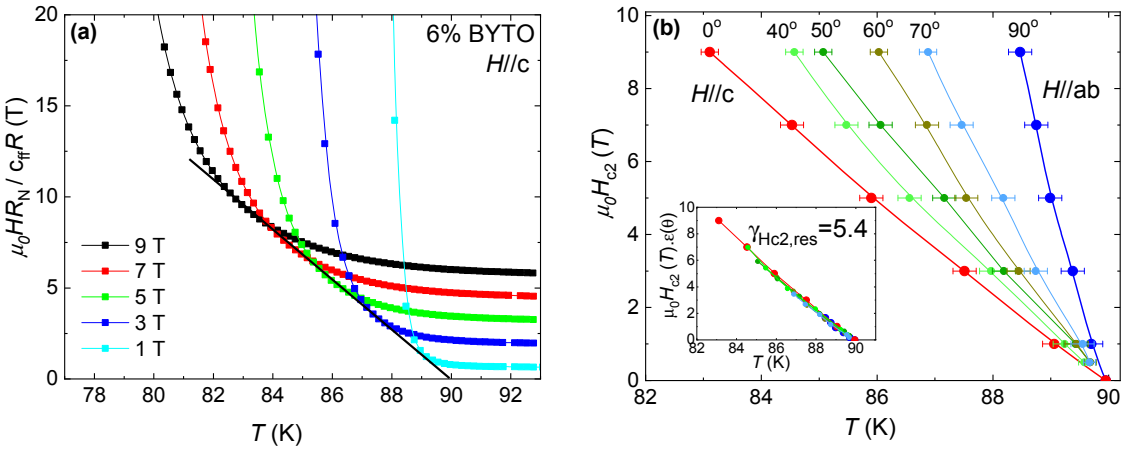

FIG. 2. (a) Determination of $H_{c2}(T)$ as the envelope of the $\mu_0 HR_N/c_{ff}R(T)$ curves, measured at different magnetic fields, applied in the direction $H//c$; (b) $\mu_0 H_{c2}(T)$ lines obtained in this way for different field orientations; Inset: Collapse of all the curves using Blatter scaling with an intrinsic $\gamma_{Hc2,res}$=5.4±0.2. (Sample: 6%BYTO nanocomposite).

where ρ_{MW} is the complex resistivity, t_s is the sample thickness and the last equation reinstates the field, angle and temperature dependences. A detailed description of the measurement setup, the method and the uncertainties involved can be found in ref.[26]. For the purposes of this paper, we will be concerned with measurements of the complex resistivity change $\Delta\rho_{MW}(H;\theta=0°)=\rho_{MW}(H;\theta=0°)-\rho_{MW}(H=0)$ and $\Delta\rho_{MW}(\mu_0 H=0.75\text{T};\theta)=\rho_{MW}(H=0.75\text{T};\theta)-\rho_{MW}(H=0;\theta)$ at fixed temperatures, see Eqs. (1) and (2).

III. LONG-RANGE VORTEX DISPLACEMENT REGIME

A. Intrinsic anisotropy $\gamma_{Hc2,HF}$

The intrinsic anisotropy can be determined from the study of the angular dependence of the upper critical field, H_{c2}. From the evaluation of the temperature-dependence $H_{c2}(T)$ under $H//c$ and $H//ab$, the coherence lengths ξ_0^{ab} and ξ_0^{c} are obtained using:

$$H_{c2}(\mathbf{H}//c)=\frac{\Phi_0}{2\pi\xi_{ab}^2}, \quad (3)$$

$$H_{c2}(\mathbf{H}//ab)=\frac{\Phi_0}{2\pi\xi_{ab}\xi_c}, \quad (4)$$

where $\xi_i(T)=\xi_0^i(1-T/T_c)^{-1/2}$ near T_c, and the intrinsic mass anisotropy is obtained as: $\gamma_{Hc2,HF}=\xi_0^{ab}/\xi_0^{c}$. In order to carry out this analysis, one approach is to determine $H_{c2}(T)$ from magnetoresistance measurements at different orientations under very high fields. The intrinsic mass anisotropy obtained in this way will be denoted $\gamma_{Hc2,HF}$. It is emphasized here that resistivity measurements must be performed over a wide region of fields to ensure the linear region, and the

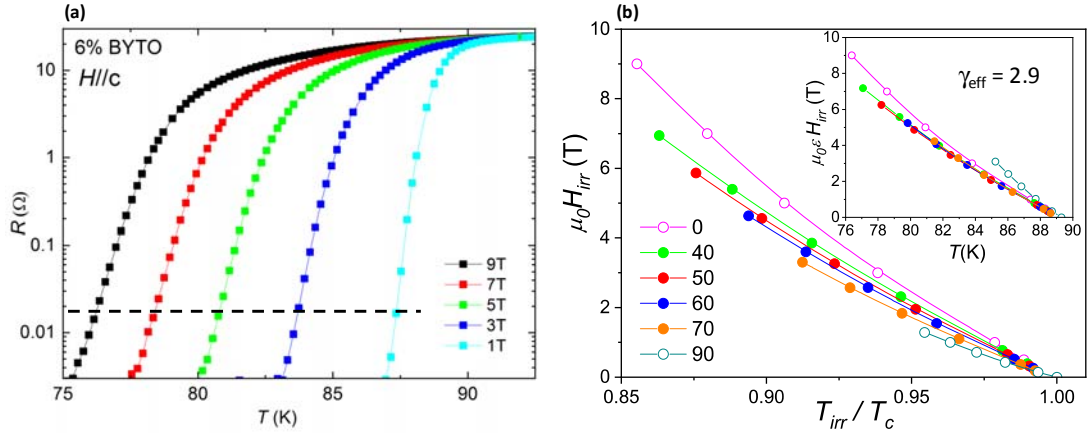

FIG. 3. (a) Resistance as a function of temperature at different magnetic fields applied in the direction $H//c$. Dashed line shows the criterium used to determine the IL; (b) Irreversibility line as a function of the reduced temperature at different magnetic field orientations. Inset: Scaling of the IL allowing the determination of the effective mass anisotropy, γ_{eff} =2.9±0.1 (Sample: 6%BYTO nanocomposite).

correct determination of H_{c2}.

In this work, we performed resistivity measurements under pulsed fields as high as 65 T in order to obtain $\gamma_{Hc2,HF}$ of two standard samples and three NCs. Figure 1a displays e.g. several $\rho(H)$ curves measured at different temperatures at $H//c$ for a 15%BYTO NC. Grey lines indicate the criterion used to determine the value of H_{c2}. In Figure 1b, H_{c2} is plotted as a function of the reduced temperature, $t=T/T_c$, for three different field orientations: 0º (**H**//c), 45º and 90º (**H**//ab). In this example, the coherence lengths obtained from Eq. (3-4) were ξ_0^{ab}=1.7 nm, ξ_0^{c}=0.32 nm and thus the intrinsic anisotropy was $\gamma_{Hc2,HF}$=5.4.

All the studied samples presented a similar intrinsic anisotropy, $\gamma_{Hc2,HF}$≈5.1-5.9, independently of the nanoparticle concentration and nanostrain induced in the sample, in agreement with earlier results reported by our group [3,10,18]. The data are summarized in the final Figure 7 (blue squares).

B. Intrinsic anisotropy $\gamma_{Hc2,res}$

The determination of $H_{c2}(T)$ from magnetoresistance measurements in ultra-high fields requires the access to a large facility, thus limiting the number of samples that can be studied. An alternative approach, proposed by Gordeev *et al.* [35,36], is to use resistive measurements in the flux-flow regime to obtain $H_{c2}(T)$. In fact, although the flux-flow resistivity is a complex matter and different expressions can be worked out depending on the microscopic mechanism adopted [37–40] many models yield $\rho_{ff} \propto H/H_{c2}$. In particular, according to the expression given by Ivlev *et al.* [41,42]:

$$\frac{\rho_{ff}(H,\theta,T)}{\rho_N(T)} = \frac{H}{c_{ff} H_{c2}(\theta,T)}, \quad (5)$$

where $\rho_N(T)$ is the normal state resistivity and c_{ff} =1.45 is a constant. When H is sufficiently larger than H_{c1}, $H_{c2}(T)$ is obtained as the envelope of the $\mu_0 H\rho_N/c_{ff}\rho(T)$ dependencies plotted at different fields applied in a fixed direction (see Figure 2a). Measurements under different magnetic field orientations allow obtaining $H_{c2}(T, \theta)$ curves (Figure 2b). As shown in the inset, all the curves collapse into a single $H_{c2}(T)\varepsilon(\theta)$ curve, when using an intrinsic $\gamma_{Hc2,res}$. Figure 2 exemplifies the procedure applied to a 6%BYTO NC, which yielded $\gamma_{Hc2,res}$=5.4. We note here that the numerical prefactor c_{ff} in Eq. (3) simplifies out in the determination of $\gamma_{Hc2,res}$, which is then independent on the specific flux-flow model adopted (although the numerical values of H_{c2} can vary).

The use of this methodology allowed us to explore the intrinsic anisotropy of a large number of thin-films and NCs of different types. Figure 7 (black circles) shows that the $\gamma_{Hc2,res}$ obtained for the 11 studied samples is virtually independent of the nanostrain, and the average intrinsic anisotropy mass value, $\gamma_{Hc2,res}$≈6.3, coincides with $\gamma_{Hc2,HF}$ within 10%.

C. Effective anisotropy γ_{eff}

Resistive measurements $\rho(H,T,\theta)$ were used to analyse the angular dependence of the irreversibility line (IL), and determine the effective anisotropy in the pinning regime. Figure 3a shows e.g. the $R(T)$ curves at different applied magnetic fields for **H**//c orientation and the determination of the irreversibility temperature, T_{irr}, for a 6% BYTO NC. As shown in Figure 3b, an excellent scaling of the IL, $H_{irr}(T_{irr}, \theta)$, is obtained for a broad range of θ when using the effective γ_{eff}=2.9. It should be noted that the IL at θ=90º and 0º do not follow the scaling since in this case we have the effect of anisotropic (1D and/or 2D) pinning centres, as a further demonstration of its different origin. As shown in Figure 7 (red stars), different from the intrinsic anisotropy mass, the effective mass shows a pronounced decay with the nanostrain, as earlier found for other NCs in our group [10].

IV. MICROWAVE, SHORT-RANGE VORTEX OSCILLATION REGIME

In order to estimate the anisotropy in the mixed state, the dc measurements are obviously limited to the regimes where fluxons move, and then give a measurable voltage. Thus, the observable regimes are either above the irreversibility line, with the dc resistivity, or in the strongly nonlinear regime, with critical current density measurements. However, when vortices are subjected to an alternating current $\boldsymbol{J_{rf}}$, the ac response can be observable also below the IL. At very high frequencies in the microwave (MW) regime, (in our case 50 GHz), vortex displacements are extremely small, much less than 1 nm[43]. Then, vortices oscillate around their equilibrium positions in their potential wells and give a measurable signal well below the IL. Measuring the high-frequency ac resistivity *vs*. the field and angle can yield the intrinsic anisotropy, here denoted as γ_{MW}, as we explain below.

We consider that vortices are subjected to the driving Lorentz force, the recall pinning force and the dissipation due to flux-flow (we neglect momentarily the flux-creep, see below), which can be described according to the well-known force equation:

$$\eta\, \boldsymbol{v} + k_p\, \boldsymbol{x} = \boldsymbol{J_{rf}} \times \Phi_0, \quad (6)$$

where η is the so-called vortex viscosity (or drag coefficient), k_p is the pinning constant (Labusch parameter) and $\boldsymbol{x}$ and $\boldsymbol{v}$ are the displacement from the equilibrium position and the

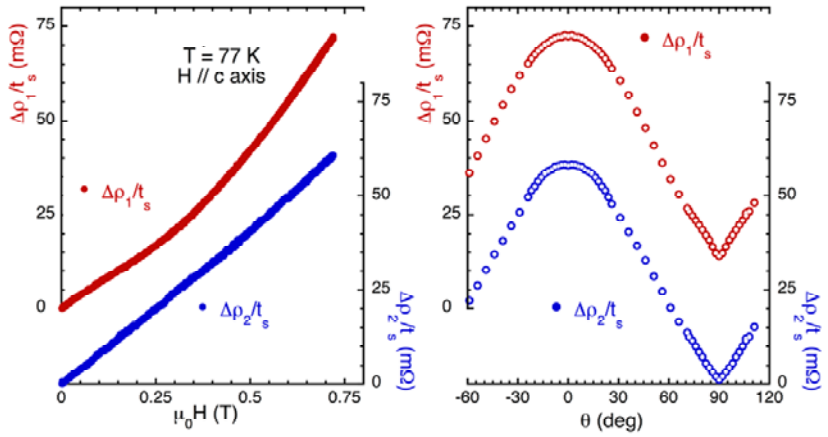

FIG. 4. (a) Microwave complex resistivity shift *vs.* applied field for a nanocomposite, $\Delta\rho_1(H,\theta=0^o)$ and $\Delta\rho_2(H,\theta=0^o)$; (b) angular dependence of the complex resistivity, $\Delta\rho_1(\mu_0 H=0.75\text{T},\theta)$ and $\Delta\rho_2(\mu_0 H=0.75\text{T},\theta)$, at a fixed field $\mu_0 H$ = 0.75 T (Sample: 6%BYTO nanocomposite).

velocity of the vortex, respectively. One may note that, by writing the recall force as $k_p\mathbf{x}$, we have approximated the potential well for each vortex as a parabolic well.

This is justified by the tiny vortex displacement from the equilibrium. Moreover, since we are dealing with a system of many vortices, one might worry about the applicability of a single-vortex equation like Eq. (6). However, although the vortex equilibrium positions are determined by a complex balance between the details of pinning and vortex-vortex interactions, such intricate framework is of almost no importance to very small oscillations: vortices do not leave their equilibrium sites, and their motion reflects: (i) the curvature of the pinning well (strength of the recall "spring", k_p), and (ii) the microscopic dissipation mechanism (flux-flow). In this framework a single-vortex dynamics is adequate to the description of the vortex motion[32,44]. Of course, the resulting vortex parameters should be intended as an average over all vortices. We stress that this is a *linear response regime*, and that the response is detectable deep in the vortex solid phase.

The response function is the complex vortex resistivity ρ_v. By recalling the definition of the flux-flow resistivity, $\rho_{ff}=\Phi_0 B/\eta$, and of the depinning frequency, $\nu_p = k_p/2\pi\eta$, one has [32]:

$$\rho_v(H,\theta)=\rho_{v1}+i\rho_{v2}=\rho_{ff}(H,\theta)\frac{1}{1-i\nu_p(H,T)/\nu}, \qquad (7)$$

where in principle all parameters depend on temperature, magnetic field and field orientation. Here ν_p marks the crossover between reactive ($\nu < \nu_p$) and dissipative ($\nu > \nu_p$) response; ρ_{ff} is the flux-flow resistivity, as it would be obtained in absence of pinning ($\nu_p \rightarrow 0$). The details of pinning are contained in ν_p. We stress that, in general, both ρ_{v1} and ρ_{v2} contain a combination of ρ_{ff} and ν_p, so that measurements of both real and imaginary parts are needed to invert Eq. (7) and obtain ρ_{ff} and ν_p. In the range of small magnetic field here reported (0-0.75T), we can safely identify the experimental $\Delta\rho$ (Eqs. (1)-(2)) with ρ_v, Eq. (7), and thus obtain ρ_{ff}.

A final note on the potential effect of flux-creep. First, we note that the measurements here presented are taken below the irreversibility line, so we expect a little -if any- contribution of flux creep to the overall response. Second, thanks to a combination of physical and analytical properties of the full expression of the vortex complex resistivity, the creep contribution can be treated as a correction of which one can estimate the weight in the form of a confidence band of the derived ρ_{ff} and ν_p. The lengthy procedure is described in detail in ref.[44]. This contribution is the main source of uncertainty on the microwave-derived anisotropy parameter γ_{MW}, reported in the final Figure 7 as uncertainty bars.

To obtain the anisotropy, we rely on the Blatter scaling applied to our microwave data for ρ_{ff}. We note that the Blatter scaling cannot apply to ν_p, as any directional source of pinning introduces an additional, extrinsic anisotropy source[45]. Indeed, as shown in Figure 5, the angular dependence of the depinning frequency, $\nu_p(\theta)$, exhibits a sharp peak at θ=90° due to ab-plane intrinsic pinning and a broader maximum at θ=0° associated to pinning at twin boundaries present in the sample. Therefore, the data do not support a scaling.

Instead, the scaling applies to ρ_{ff} which is exclusively related to intrinsic processes. So, microwave measurements can estimate the intrinsic anisotropy, via the extraction of ρ_{ff} in a region of the *H-T* phase diagram otherwise inaccessible. The capability of this technique to actually access the intrinsic anisotropy has been first demonstrated in ref. [45], where a PLD YBCO film with 5% mol $BaZrO_3$ addition was found to have $\gamma = 5$.

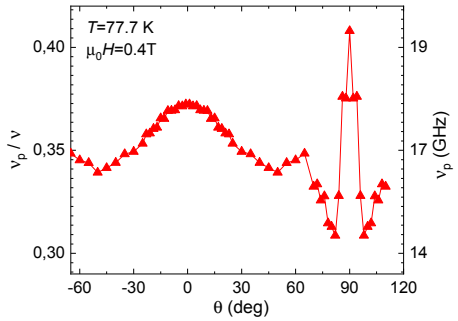

FIG. 5. Depinning frequency ν_p, normalized to the measuring frequency (left axis), and absolute (right): the sharp peak at θ=90° is due to intrinsic pinning, while the broader maximum at θ=0° is associated to twin boundary pinning. The angular dependence reflects all the details of at least two sources of directional pinning, acting in a competitive way, so that ν_p cannot be reconciled to a scaling function. (Sample: YBCO thin-film, γ_{MW}=5.1).

We note here a technical complication: our system makes use of a cylindrical symmetric resonator, and thus the Lorentz force on flux lines ($\boldsymbol{J}_{rf} \times \Phi_0$ in Eq. (6)) changes with the same angle θ that the field makes with the *c*-axis. The expected angular scaling then contains $\varepsilon(\theta)$ and the angular variation of the Lorentz force $L(\theta)$. It is worth stressing that the specific form of $L(\theta)$ is written under the assumption that vortex lines are parallel to the externally applied magnetic field. Although in very thin films and at low flux densities (fields very close to the lower critical field)[46,47,48] this assumption can be debated, the present measurements are taken in a very different field range: the measurements for tilted angles are taken in fields much larger than the (anisotropic) penetration field, so that the field almost fully penetrates (small vortex spacing regime). As a consequence, the tilt angle of the vortices follows the tilt angle of the applied field[46,47]. As a further reinforcement, we also note that our angular results (see Fig. 5c below) are independent on the field intensity, consistently with an average fluxon direction which is aligned with the external field (negligible boundary effects). It turns out that the scaled field $H_{eff}=H\varepsilon(\theta)$ is replaced by $H_{eff}=H\varepsilon(\theta)L(\theta)$, with[49]:

$$L(\theta)=\frac{\frac{1}{2}\gamma_{MW}^{-2}\sin^2\theta+\cos^2\theta}{\gamma_{MW}^{-2}\sin^2\theta+\cos^2\theta}. \qquad (8)$$

Eq. (8) is valid when the flux-flow resistivity is almost linear with H [49] (as it is the case here). We define the scaling function:

$$f(\theta)=1/\varepsilon(\theta)L(\theta), \qquad (9)$$

such that the effective field reads $H_{eff}=H/f(\theta)$. We note that this is still a one-parameter function, where γ_{MW} is the intrinsic, microwave-obtained mass anisotropy. Combining the ρ_{ff} data as a function of the field with H//c, and as a function of the angle at a fixed field H_0, we derive the scaling function as graphically depicted in Figs. 6a and 6b. The procedure can be repeated at different H_0 to ensure the independence of $f(\theta)$ on the applied field (obviously, this is made using additional data sets like those reported in Figs. 4b and 6b, at different H_0). We then compared the experimental $f(\theta)$ with Eq. (8). In Figure 6c we report the so-obtained scaling function, together with the result of Eq. (8). We stress that this equation does not contain adjustable parameters, since $f(0°)=1$ and $f(90°)=2\gamma$ (the factor 2 comes from the Lorentz force contribution to f, Eq. (7)), so the agreement of the experimental $f(\theta)$ with the theoretical expression, Eq. (8), which is based on the Blatter scaling, is a

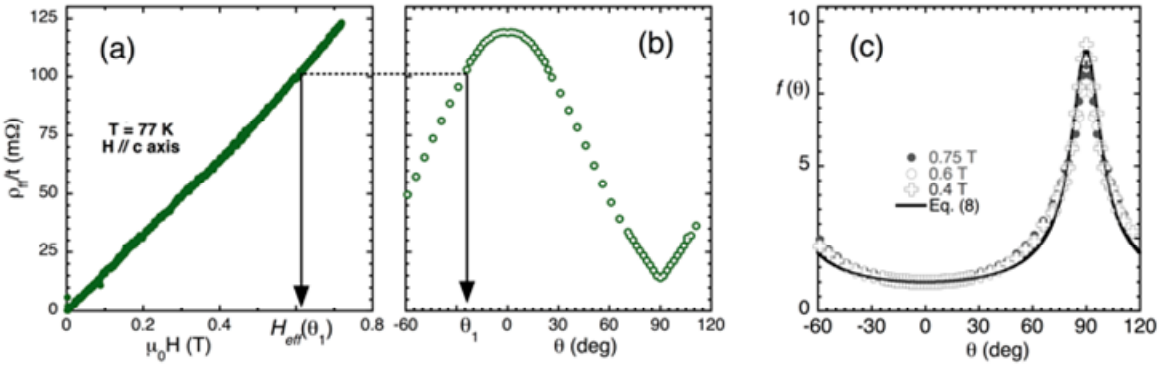

FIG. 6. (a) Field dependence of the flux-flow resistivity, derived from the data of Figure 4 by means of Eq. (7); (b) Angular dependence of the flux-flow resistivity measured at constant magnetic field $\mu_0 H_\theta$=0.75 T. The procedure to obtain the effective field H_{eff} at a sample angle θ_1 is depicted graphically. Repeating the procedure at all angles one gets $H_{eff}(\theta)$ and $f(\theta)= H_0/H_{eff}$; (c) Scaling functions $f(\theta)$ as derived from the data in panels (a) and (b) (grey full dots) and at two other fields H_0, and the theoretical expression Eq. (8), black line, calculated with γ_{MW}=4.5 in this sample. (Sample: 6%BYTO nanocomposite).

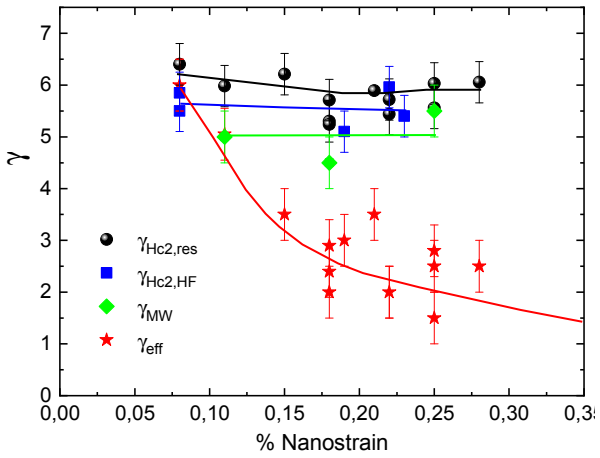

FIG. 7. Dependence of effective anisotropy factor (γ_{eff}) and the intrinsic anisotropy factors, determined from resistive measurements in high fields ($\gamma_{Hc2,HF}$), resistive measurements ($\gamma_{Hc2,res}$) and microwave measurements (γ_{MW}), as a function of the nanostrain (%) for the studied YBCO thin-films and NCs. (Nanostrain error bar omitted for sake of clarity is ±0.02%).

demonstration of the applicability of the scaling to our data for ρ_{ff}. From the angular scaling of the flux-flow resistivity, obtained in the vortex solid by means of microwave-induced vortex oscillations, we finally get the mass anisotropy. The intrinsic mass anisotropy found for all the studied samples was similar, γ_{MW}=4.5-6, see Figure 7 (green diamonds), confirming that the introduction of NPs in YBCO does not induce significant changes in the electronic state.

V. DISCUSSION AND CONCLUSIONS

Figure 7 summarizes the intrinsic mass anisotropy, determined by the different methods ($\gamma_{Hc2,HF}$, $\gamma_{Hc2,res}$, γ_{MW}), and the effective anisotropy factor (γ_{eff}) as a function of the nanostrain for all the studied samples. The following conclusions can be drawn:

The intrinsic anisotropy factor determined from resistivity measurements, $\gamma_{Hc2,res,}$ is similar to $\gamma_{Hc2,HF}$ values obtained from experiments in pulsed high fields. Therefore, the resistivity approach is an attractive method to investigate the intrinsic anisotropy of many samples, not requiring a large facility. The flux-flow, intrinsic anisotropy obtained from MW (γ_{MW}) coincides within the uncertainty error with that obtained from long-range direct current measurements. In every case, the intrinsic anisotropy is independent of the % nanostrain. The results allow us to conclude that in our CSD-grown YBCO thin-films, nanostructuration, increasing the associated nanostrain does not change the underlying electronic state. The values for the intrinsic anisotropy ratio are close to commonly accepted values, and they do not report anomalously small values. This is consistent with the difficulty of reaching a dirty limit that would have disorder in a scale smaller than the coherence length. In contrast, the effective anisotropy (γ_{eff}) decreases in correlation with the increase of % nanostrain in YBCO, achieved through the inclusion of the nanoparticles.

ACKNOWLEDGEMENTS

We acknowledge financial support from Spanish Ministry of Economy and Competitiveness through the "Severo Ochoa" Programme for Centres of Excellence in R&D (SEV-2015-0496), COACHSUPENERGY project (MAT2014-51778-C2-1-R, co-financed by the European Regional Development Fund), NANOCOHYBRI project (Cost Action CA 16218), DWARFS project (MAT2017-83468-R) and from the Catalan Government with 2014-SGR-753. ICMAB Scientific and Technical Services are acknowledged. Work at LANL (B.M. and L.C.) as supported by the U.S. DOE, Office of Basic Energy Science, Materials Sciences and Engineering Division. Work by F.F.B and work performed at NHMFL pulsed field facility at Los Alamos National Laboratory was founded by NSF by Grant number 1157490/1644779.

[1] J.P. Feighan, A. Kursumovic, and J.L. MacManus-Driscoll, Supercond. Sci. Technol. **30**, 123001 (2017).
[2] B. Maiorov, G. Nieva, and E. Osquiguil, Phys. Rev. B **61**, 12427 (2000).
[3] A. Baily, B. Maiorov, H. Zhou, F.F. Balakirev, M. Jaime, R. Foltyn, and L. Civale, Phys. Rev. Lett **100**, 027004 (2008).
[4] G. Blatter, V.B. Geshkenbein, and A.I. Larkin, Phys. Rev. Lett **68**, 875 (1992).
[5] L. Civale, B. Maiorov, A. Serquis, S.R. Foltyn, Q.X. Jia, P. Arendt, H. Wang, J.O. Willis, J.Y. Coulter, T.G. Holesinger, M.W. MacManus-Driscoll, J.L. Rupich, W. Zhang, and X. Li, Phys. C **412–414**, 976 (2004).
[6] J. Gutierrez, a Llordes, J. Gazquez, M. Gibert, N. Roma, S. Ricart, a Pomar, F. Sandiumenge, N. Mestres, T. Puig, and X. Obradors, Nat. Mater. **6**, 367 (2007).
[7] A. Palau, F. Valles, V. Rouco, M. Coll, Z. Li, C. Pop, B. Mundet, J. Gazquez, R. Guzman, J. Gutierrez, X. Obradors, and T. Puig, Supercond. Sci. Technol. **31**, (2018).
[8] L. Civale, B. Maiorov, A. Serquis, J. Willis, J. Coulter, H. Wang, J. Q., P. Arendt, M. Jaime, J. MacManus-Driscoll, M. M., and S. Foltyn, J. Low Temp. Phys. **135**, 87 (2004).
[9] L. Civale, B. Maiorov, A. Serquis, J.O. Willis, J.Y. Coulter, H. Wang, Q.X. Jia, P.N. Arendt, J.L. MacManus-Driscoll, M.P. Maley, and S.R. Foltyn, Appl. Phys. Lett. **84**, 2121 (2004).
[10] A. Llordés, A. Palau, J. Gázquez, M. Coll, R. Vlad, A. Pomar, J. Arbiol, R. Guzmán, S. Ye, V. Rouco, F. Sandiumenge, S. Ricart, T. Puig, M. Varela, D. Chateigner, J. Vanacken, J. Gutiérrez, V. Moshchalkov, G. Deutscher, C. Magen, and X. Obradors, Nat. Mater. **11**, 329 (2012).
[11] M. Erbe, J. Hänisch, R. Hühne, T. Freudenberg, A. Kirchner, L. Molina-Luna, C. Damm, G. Van Tendeloo, S. Kaskel, L. Schultz, and B. Holzapfel, Supercond. Sci. Technol. **28**, (2015).
[12] P. Cayado, B. Mundet, H. Eloussifi, F. Vallés, M. Coll, S. Ricart, J. Gázquez, A. Palau, P. Roura, J. Farjas, T. Puig, and X. Obradors, Supercond. Sci. Technol. **30**, (2017).
[13] A. Xu, V. Braccini, J. Jaroszynski, Y. Xin, and D.C. Larbalestier, Phys. Rev. B **86**, 115416 (2012).

[14] A. Xu, F. Kametani, and D. Larbalestier, Appl. Phys. Lett. **106**, 052603 (2015).
[15] M. Miura, B. Maiorov, F.F. Balakirev, T. Kato, M. Sato, Y. Takagi, T. Izumi, and L. Civale, Sci. Rep. **6**, (2016).
[16] V. Rouco, A. Palau, R. Guzman, J. Gazquez, M. Coll, X. Obradors, and T. Puig, Supercond. Sci. Technol. **27**, 125009 (2014).
[17] H. Huhtinen, H. Palonen, M. Malmivirta, R. Jha, S.V.P. Awana, and P. Paturi, J. Phys. Conf. Ser. **507**, 012020 (2014).
[18] M. Miura, S.A. Baily, B. Maiorov, L. Civale, J.O. Willis, K. Marken, T. Izumi, K. Tanabe, and Y. Shiohara, Appl. Phys. Lett. **96**, 072506 (2010).
[19] M. Malmivirta, H. Palonen, S. Inkinen, L.D. Yao, J. Tikkanen, H. Huhtinen, R. Jha, V.P.S. Awana, S. van Dijken, and P. Paturi, J. Pjys.Condens.Matter **28**, 175702 (2016).
[20] M. Malmivirta, H. Palonen, H. Huhtinen, and P. Paturi, J. Phys. Conf. Ser. **507**, 012030 (2014).
[21] H. Palonen, H. Huhtinen, M.A. Shakhov, and P. Paturi, Supercond. Sci. Technol. **26**, 045003 (2013).
[22] R. Willa, A.E. Koshelev, I.A. Sadovskyy, and A. Glatz, Supercond. Sci. Technol. **31**, 014001 (2018).
[23] A.E. Koshelev and A.B. Kolton, Phys. Rev. B **84**, 104528 (2011).
[24] C.J. Van Der Beek, M. Konczykowski, and R. Prozorov, Supercond. Sci. Technol. **25**, 084010 (2012).
[25] N. Haberkorn, M. Miura, J. Baca, B. Maiorov, I. Usov, P. Dowden, S.R. Foltyn, T.G. Holesinger, J.O. Willis, K.R. Marken, T. Izumi, Y. Shiohara, and L. Civale, Phys. Rev. B - Condens. Matter Mater. Phys. **85**, 1 (2012).
[26] N. Pompeo, K. Torokhtii, and E. Silva, Meas. Sci. Rev. **14**, 64 (2014).
[27] L.F. Chen, C.K. Ong, C.P. Neo, V. V Varadan, and V.K. Varadan, Wiley (2004).
[28] N. Pompeo, K. Torokhtii, and E. Silva, in *Proc. I2MTC, Torino, May 22-25 (2017), Instrum. Meas. Technol. Conf. (I2MTC), 2017 IEEE Int. Pp.1-6, 11-14 May 2015* (2017), pp. 1–6.
[29] M.W. Coffey and J.R. Clem, Phys. Rev. B **46**, 11757 (1992).
[30] M.W. Coffey and J.. Clem, Phys. Rev. B **45**, 10527 (1992).
[31] M.W. Coffey, Phys. Rev. B **47**, 12284 (1993).
[32] J.I. Gittleman and B. Rosenblum, Phys. Rev. Lett. **16**, 734 (1966).
[33] N. Pompeo and E. Silva, IEEE Trans. Appl. Supercond. **28**, 8201109 (2018).
[34] N. Pompeo, L. Muzzi, V. Galluzzi, R. Marcon, and E. Silva, Supercond. Sci. Technol. **20**, 1002 (2007).
[35] S.N. Gordeev, A.P. Rassau, R.M. Langan, P.A.J. Groot, V.B. Geshkenbein, R. Gagnon, and L. Taillefer, Phys. Rev. B **60**, 10477 (1999).
[36] R.M. Langan, S.N. Gordeev, M. Oussena, P.A.J. de Groot, A.G.M. Jansen, R. Gagnon, and L. Taillefer, Phys. C Supercond. **313**, 294 (1999).
[37] L.P. Gor'kov and N.B. Kopnin, Sov. Phys.-Usp. **18**, 496 (1975).
[38] A.I. Larkin and Y.N. Ovchinnikov, *Nonequilbirum Superconductivity-Modern Problems in Condensed Matter Sciences, Vol. 12*, Elsevier S (1986).
[39] N.B. Kopnin, *Theory of Nonequilibrium Superconductivity* (2001).
[40] A. Vargunin and M.A. Silaev, Phys. Rev. B **96**, 214507 (2017).
[41] B.I. Ivlev and N.B. Kopnin, Europhys. Lett. **15**, 349 (1991).
[42] B.I. Ivlev and N.B. Kopnin, Phys. Rev. B **42**, 10052 (1990).
[43] W.J. Tomasch, H.A. Blackstead, S.T. Ruggiero, P.J. McGinn, J.R. Clem, K. Shen, W. Weber, and D. Boyne, Phys. Rev. B **37**, 9864 (1988).
[44] N. Pompeo and E. Silva, Phys. Rev. B - Condens. Matter Mater. Phys. **78**, 1 (2008).
[45] N. Pompeo, A. Augieri, K. Torokhtii, V. Galluzzi, G. Celentano, and E. Silva, Appl. Phys. Lett. **103**, 022603 (2013).
[46] E.H. Brandt, Phys. Rev. B **48**, 6699 (1993).
[47] Y.A. Martynovich, J. Exp. Theor. Phys. **78**, 489 (1994).
[48] D.A. Savinov, Supercond. Sci. Technol. **25**, 015003 (2012).
[49] N. Pompeo, J. Appl. Phys. **117**, 103904 (2015).